Journal of Materials Chemistry A

Chemomechanical effect of reduced graphene oxide encapsulation on hydrogen storage performance of Pd nanoparticles

Journal:	*Journal of Materials Chemistry A*
Manuscript ID	TA-ART-02-2021-001240.R1
Article Type:	Paper
Date Submitted by the Author:	30-Mar-2021
Complete List of Authors:	Kim, Daeho; Korea Advanced Institute of Science and Technology, Department of Materials Science and Engineering Koh, Jinseok; Korea Advanced Institute of Science and Technology, Department of Chemical and Biomolecular Engineering Kang, ShinYoung; Lawrence Livermore National Laboratory Heo, Tae Wook; Lawrence Livermore National Laboratory, Materials Science Division Wood, Brandon; Lawrence Livermore National Laboratory Cho, Eun Seon; Korea Advanced Institute of Science and Technology, Department of Chemical and Biomolecular Engineering Han, Seung Min; Korea Advanced Institute of Science and Technology, Department of Materials Science and Engineering

ARTICLE

Chemomechanical effect of reduced graphene oxide encapsulation on hydrogen storage performance of Pd nanoparticles†

Received 00th January 20xx,
Accepted 00th January 20xx

DOI: 10.1039/x0xx00000x

Daeho Kim,[§a] Jinseok Koh,[§b] ShinYoung Kang,*[c] Tae Wook Heo,[c] Brandon C. Wood,[c] Eun Seon Cho*[b] and Seung Min Han*[a]

Primary chemomechanical impacts of confinement on hydrogen storage performance are studied using a nanolaminate structure where the reduced graphene oxide (rGO) encapsulates palladium (Pd) nanoparticles. Three contributing factors are identified that can alter the reaction enthalpy: nanosizing, chemical interaction with the encapsulant, and mechanical stress induced strain from a combination of clamping force and lateral pulling force exhibited on the Pd nanoparticles. The mechanical contributions are quantified by combining transmission electron microscopy, *ab initio* computations, and continuum elasticity theory, from which the encapsulation is found to exert an additional strain of 4.96% and 2.99% before and after hydrogen absorption, respectively, increasing the Pd and Pd hydrides (PdH_x) reaction enthalpy by 0.9-2.4 kJ (mol H_2)$^{-1}$. The effect of the chemical interaction with rGO also raises the reaction enthalpy by up to 1.6 kJ (mol H_2)$^{-1}$, while the nanosizing effect decreases the reaction enthalpy. The three contribution factors on the reaction enthalpy are found to be of similar in magnitude, where the net effect is in agreement with the measured enthalpy increase of 3.7 kJ (mol H_2)$^{-1}$ from the bulk value. Hydrogen absorption kinetics and capacity also improved, which is attributed to facile nucleation of the hydrogen-rich phase enabled by the inhomogeneous strain distribution over the encapsulated PdH_x nanoparticles. This results demonstrate that chemomechanical effect can be controlled in the nanolaminate structure, providing an ideal template for tuning hydrogen storage performance.

Introduction

An ongoing need for clean, sustainable, and diversified energy has led to intense interest in hydrogen as an alternative energy carrier.[1] Hydrogen provides a potential for an inexhaustible supply and carbon-free utilization with higher gravimetric energy density than other known chemical fuels,[1,2] allowing for use in eco-friendly power applications such as fuel cells for clean transportation.[3] Metal hydrides are considered as a promising candidate for solid-state hydrogen storage,[4] offering high gravimetric and volumetric energy density at far lower pressures compared to conventional tanks;[2] however, there remains a technical challenge due to the sluggish kinetics and undesired high operating temperatures for hydrogen sorption.[5]

Recent advances have suggested a new design for storage materials through nanoconfinement engineering, in which interactions of nanoscale particles with confining media and/or inclusion of intrinsic defects alter hydrogen storage kinetic and thermodynamic properties.[6] In practice, these changes can arise from a variety of physical factors, including surface and interface effects[7] that are enhanced upon nanosizing, the chemical interaction with the host, and mechanical stress imposed by the confining medium. Nevertheless, a definitive relationship between the properties of materials under nanoconfinement and their resulting impacts on hydrogen sorption have not been conclusively elucidated. This limits reproducibility and broad adaption to other metal hydrides. A comprehensive understanding of the structure-property relationship for confined metal hydrides is therefore highly desirable for a rational design of storage materials with optimized hydrogen sorption characteristics.

In numerous reported energy-related studies, nanostructured metals with a size less than 10 nm have demonstrated substantially altered stability and functional characteristics when confined within different kinds of host matrices, such as polymers and carbon materials.[8,9] For example, Yamauchi *et al.*[9] revealed that narrowed conduction bandwidth in Pd nanoparticles of less than 10 nm leads to significant changes in hydrogen absorption properties, such as a decrease in the heat of hydride formation. Cheung *et al.*[10] used theory to suggest an enhancement of hydrogen storage performance in the nanoscale magnesium (Mg) and magnesium hydrides (MgH_2) system, resulting from a nanosizing effect

[a] *Department of Materials Science and Engineering, Korea Advanced Institute of Science and Technology (KAIST), Daejeon, 34141, Republic of Korea, E-mail: smhan01@kaist.ac.kr*
[b] *Department of Chemical and Biomolecular Engineering, Korea Advanced Institute of Science and Technology (KAIST), Daejeon, 34141, Republic of Korea, E-mail: escho@kaist.ac.kr*
[c] *Lawrence Livermore National Laboratory, Livermore, CA 94550, United States, E-mail: kang10@llnl.gov*

† Electronic Supplementary Information (ESI) available: Additional experimental data and computational details of atomistic simulation procedure. See DOI: 10.1039/x0xx00000x

§ D. K. and J. K. contributed equally to this work.

found only in a certain range of cluster size; this study was later confirmed by an observed decrease in the desorption temperature of MgH_2 nanoparticles of less than 7 nm.[5]

The direct chemical and mechanical role of host materials and encapsulants has also been explored. For instance, graphene derivatives have been reported to act as a catalyst to reduce the activation energy required for hydrogen sorption in Pd.[11,12] In addition, a recent study by Cho *et al.*[13] showed that metal nanoparticles (mNP) encapsulated with rGO exhibit improved oxidation resistance by allowing selective permeation of hydrogen molecules through the rGO capping layers.[14,15] For Mg encapsulated within rGO,[13] it has further been suggested that confinement can cause mechanical stresses to build up in the Mg nanoparticles, in turn which is expected to have the effect of lowering the reaction enthalpy and activation energy of hydrogen absorption and desorption. Given that the synthesized Mg nanoparticles can be as small as a few nanometers,[16] nanoparticles can also be easily strained as a result of the rGO encapsulation.[17]

In this study, we incorporate the concept of rGO/mNP/rGO nanolaminates to isolate, diagnose, and quantify the various chemomechanical impacts of encapsulation on metal hydrides for hydrogen storage. For the hydrogen storage material, we use Pd, which has long been regarded as an ideal material for fundamental studies due to its mild hydriding conditions and resistance to oxide contamination.[18] Our approach combines fabrication and hydrogen sorption testing of rGO/Pd/rGO nanolaminates, detailed strain measurements using high-resolution transmission electron microscopy (HRTEM), and comprehensive theoretical analysis based on first-principles calculations and microelasticity. We point out that multiple previous studies have focused on unraveling the change of hydrogen sorption thermodynamics and kinetics for PdH_x governed by nanostructuring, including the concomitant intrinsic strain effect in the absence of an external confining medium.[19,20] Instead, ours is the first thorough analysis of PdH_x that focuses on the specific effect of the encapsulant, which acts in concert with nanosizing to alter hydrogen storage properties (Scheme 1). Beyond the specific impacts on Pd, our integrated synthesis-characterization-theory framework provides an excellent basis for obtaining a deeper general understanding of nanoscale chemomechanics, which is an underexplored factor for tuning hydrogen storage properties in various confined metal hydride systems.

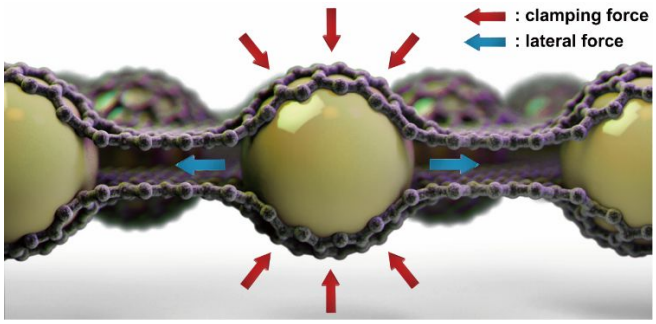

Scheme 1 Schematic illustration of rGO/Pd/rGO nanolaminates showing rGO layer wrapped around Pd nanoparticles. Red and blue arrows indicate the clamping force, and lateral force imposed by rGO layer, respectively.

Experimental section

Materials

Palladium chloride ($PdCl_2$, 99%), palladium acetylacetonate ($Pd(acac)_2$, 99%), hydrochloric acid (HCl, 36.5-38.0%), oleylamine (OAm, 70%), and borane tert-butylamine complex (BTB, 97%) were purchased from Sigma-Aldrich. Graphene oxide (GO) was purchased from Standard Graphene Inc., and deionized (DI) water was used in all synthesis.

rGO/Pd/rGO nanolaminates synthesis

Pd nanocrystals encapsulated by rGO sheets were synthesized by modifying a previously reported work.[21] 240 mg of GO powder was dispersed in 300 mL of 5.63 mM H_2PdCl_4 solution (H_2PdCl_4 solution was prepared by dissolving 302.8 mg of $PdCl_2$ and 277.6 μL of HCl in 300 mL of DI water, followed by magnetic stirring for 1 day) and then sonicated for 3 h. The obtained product was centrifuged at 10,000 rpm for 20 min, washed with DI once, and dried at 60 °C in a vacuum oven overnight. The resulting product was then reduced in a tube furnace at 300 °C for 2 h under 4% H_2 /96% N_2 gas flow.

Pd nanoparticles synthesis

Pd nanoparticles without rGO covering (bare-Pd) were also prepared by modifying a method published earlier to verify the structural effects of rGO sheets.[22] 375 mg of $Pd(acac)_2$ powder was dispersed in 75 mL of OAm and the mixture solution was stirred at 60 °C for 10 min under a nitrogen flow. 750 mg of BTB powder was dispersed in 20 mL of OAm and quickly added into the mixture solution. When the colorless solution turned to dark brown, it was heated to 90 °C and kept for 1 h. The product was washed with ethanol several times and dried under vacuum overnight.

TEM analysis

Powder sample was dispersed in the ethanol solution and drop casted on 300 mesh lacey carbon TEM grids. Conventional HRTEM images were taken with a Titan cubed G2 60-300 (FEI) at 300 kV equipped with double spherical aberration (Cs)-correctors (probe and image Cs-correctors). HRTEM analysis was performed for determining the interplanar spacing of Pd nanoparticles in rGO/Pd/rGO nanolaminates. Fast Fourier transform (FFT) analysis was performed using Gatan Micrograph Suite software (GMS3) (Gatan Inc.), and at the same magnification, displacement calibration was performed on (111) Si single crystal substrates. To confirm that the rGO layers were encapsulating around the Pd nanoparticles, a cross-section specimen was prepared using an ultra-microtome (LEICA Ultracut UCT EM UC7). rGO/Pd/rGO nanolaminates powder was embedded in CaldoFix-2 resin at 50 °C for 24 h in the furnace, cut into 50 nm thickness section with an ultra-microtome, and then placed on a 300 mesh lacey carbon grid. Cross-section TEM images were taken at 80 kV since the thin cross-sectioned sample was damaged at the high acceleration voltage.

X-ray diffraction

Powder X-ray diffraction (XRD) was performed with a Rigaku SmartLab High Resolution Powder X-ray diffractometer using CuK_α radiation source (λ = 1.5406 Å). The θ-2θ scan with angle ranging from 20° to 90° with a 0.01° step size at a scan rate of 5°/min was performed, and the data was analysed using PDXL (Rigaku) software.

Composition analysis

Chemical mapping with energy-dispersive X-ray spectroscopy (EDS) was performed using the Titan cubed G2 at 300 kV, which is equipped with four integrated silicon-drift EDS detectors (ChemiSTEM™ technology) at a collection solid angle of 0.7 sr. During elemental mapping, Pd-L_α (2.8 keV), O-K_α (0.5 keV) lines were selected. The probe current was adjusted to be 300 pA with a scanning time of 300s. X-ray photoelectron spectroscopy (XPS) measurements were performed to determine the morphology using a Thermo VG Scientific spectrometer with an Al-K_α source.

Preparation of rGO/PdH_x/rGO nanolaminates

As-synthesized rGO/Pd/rGO nanolaminates were hydrided using a HyEnergy Sieverts PCT Pro-2000 at 100 °C under 15 bar of H_2 pressure for 24 h. Right after the hydrogen absorption, the products were pre-treated for further characterization.

Hydrogen absorption measurements

Hydrogen absorption kinetic measurements were carried out using a HyEnergy Sieverts PCT Pro-2000 at 100 °C under 2.2 bar of H_2 pressure. Pressure Concentration Temperature (PCT) measurements were performed with in-house set-up at three different temperatures. All measurements were calculated based on Pd metal loadings in the composites to elucidate the structural effect of rGO sheets. The Pd content in rGO/Pd/rGO samples was determined by inductively coupled plasma atomic emission spectroscopy (ICP-AES) using an OPTIMA 7300 DV.

Atomistic simulations

Classical molecular dynamics simulations using the embedded-atom method (EAM) potential and DFT computation were performed for the interatomic distance prediction. Spherical nanoparticles with diameter 1-6 nm were constructed, and the nanoparticle geometry and atomic positions were optimized. The average Pd-Pd interatomic distance, d_{nano}, was compared to the reference Pd-Pd interatomic distance in bulk, d_{bulk}. Predicted changes in the interatomic distance, *i.e.,* $(d_{nano} - d_{bulk})/d_{bulk} \times 100$ (%), were interpolated from the DFT calculation data for small particles (smaller than 2 nm) to the EAM potential data for larger particles, and the result served as a reference to calculate the strains induced by rGO encapsulation without the nanosizing effect.

On the other hand, the bulk moduli of 1.6 nm Pd and 1.4 nm PdH nanoparticles were predicted as a representative elastic property in nanoscale. Quantum mechanical volume and energy under a series of external stress calculated in DFT computation with Environ code extension[23,24] were plugged into the Murnaghan equation of state[25] to compute the bulk moduli of nanoparticles. Bulk moduli of 3 nm Pd and PdH particles were estimated using the interpolation trend and the full anisotropic elastic stiffness tensor C was scaled assuming the same ratio predicted in the bulk modulus K, *i.e.* $C_{nano} = C_{bulk} \cdot K_{nano}/K_{bulk}$. In addition, the chemical interaction between rGO and PdH_x nanoparticle is modeled using the simplified interface between graphene and spherical Pd (or PdH) particle in the DFT.

Strain energy calculations

The strain energy can be calculated by the following equation.

$$\Delta H_{strain} = \tfrac{1}{2} V_0 (C_{11}\varepsilon_{11}^2 + C_{22}\varepsilon_{22}^2 + C_{33}\varepsilon_{33}^2 + C_{12}\varepsilon_{12}^2 + C_{23}\varepsilon_{23}^2 + C_{31}\varepsilon_{31}^2)$$

where V_0 is the molar volume in equilibrium, C_{ij} (i,j = 1-3) is the elastic stiffness tensor, and ε_{ij} (i,j = 1-3) is strain tensor. Depending on the orientations of PdH_x nanoparticles with respect to rGO, this equation can be simplified to equation (1) or (2).

$$\Delta H_{strain} \approx \tfrac{1}{2} V_0 C_{11} (2\varepsilon_{in\text{-}plane}^2 + \varepsilon_{out\text{-}of\text{-}plane}^2) \quad (1)$$

$$\Delta H_{strain} \approx \tfrac{1}{2} V_0 C_{12} (2\varepsilon_{in\text{-}plane}^2 + \varepsilon_{out\text{-}of\text{-}plane}^2) \quad (2)$$

The reaction enthalpy shifts by the strain energy is approximated to $\Delta H_{strain}^{Pd} - \Delta H_{strain}^{PdH}$.

Results and discussion

Characterization of rGO/Pd/rGO nanolaminates

Synthesized rGO/Pd/rGO nanolaminates were first imaged in the TEM to determine the morphology. The low magnification TEM image (Fig. 1a) indicates that the rGO sheets are several microns in size, and the high magnification TEM image (Fig. 1b) revealed that spherical Pd nanoparticles were dispersed within rGO sheet. Particle size distributions were calculated using ImageJ software based on at least 1,000 nanoparticles. The upper inset of Fig. 1b confirms that the Pd particles were 3.32±0.51 nm in diameter, and the particles in hydrided rGO/PdH_x/rGO nanolaminates were 3.42±0.44 nm in diameter (Fig. S1a). To confirm that the rGO layers were encapsulating the Pd nanoparticles, a powder sample of rGO/Pd/rGO nanolaminates was solidified into the resin, and the specimen was cut using ultra-microtome to image the sandwiched structure in cross-section by TEM. As shown in Fig. 1c, the Pd nanoparticle is wrapped by rGO layers on either side, thereby

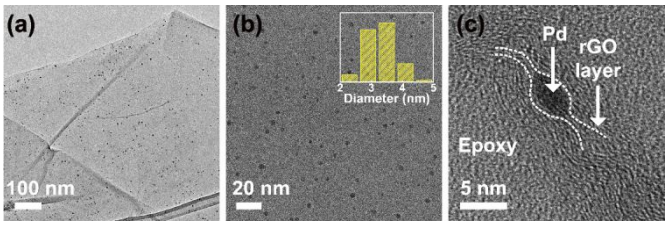

Fig. 1 TEM images of rGO/Pd/rGO nanolaminates at (a) low magnification and (b) high magnification. The inset indicates the size distribution of the Pd nanoparticles. (c) Cross-section TEM image of rGO/Pd/rGO nanolaminates. Pd nanoparticle is encapsulated by rGO layers on either side.

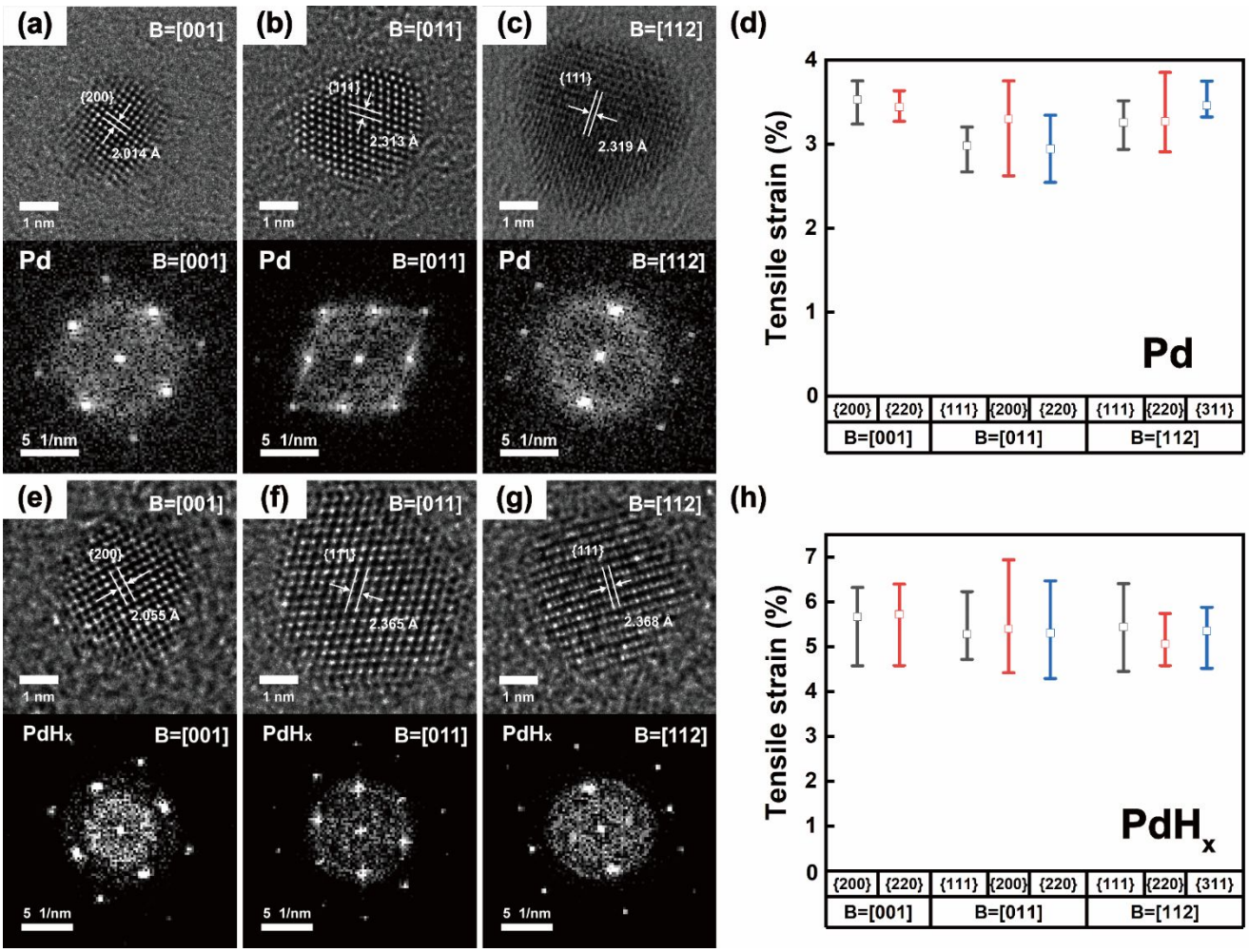

Fig. 2 HRTEM (upper) and FFT (lower) images of Pd and PdH_x with zone axes of (a,e) [001], (b,f) [011], (c,g) [112]. (d,h) The in-plane strain for [001], [011], [112] zone axes of Pd and PdH_x encapsulated by rGO layers in the nanolaminates determined for different orientations for each zone axis (versus bulk Pd reference). Tensile strain applied to PdH_x nanoparticles includes both the strain induced by rGO as well as the lattice expansion of the Pd nanoparticles as it undergoes hydrogen absorption.

confirming the morphology of rGO/Pd/rGO nanolaminates as represented in Scheme 1 (The original cross-section TEM image of Fig. 1c without dashed lines is shown in Fig. S2). Synthesized rGO/Pd/rGO nanolaminates were composed of zero-valent Pd state nanoparticles and wrapped by rGO layers as supported by XPS, XRD, and EDS analysis (Fig. S3-S6).

Strain analysis of rGO/Pd/rGO nanolaminates

In the rGO/Pd/rGO nanolaminates, Pd nanoparticles are sandwiched between the rGO layers and expected to be strained. First, the Pd nanoparticles should be compressed relative to their bulk counterpart due to the effect of surface tension, as has been reported.[26,27] Second, the rGO encapsulation should cause additional strain to be applied on the Pd nanoparticles, which can change the hydrogen sorption properties. Therefore, we analysed the strain induced in the Pd nanoparticles due to rGO encapsulation using the interplanar spacing difference of individual Pd nanoparticles.

In this study, analysed Pd nanoparticles are face centered cubic (FCC) single crystals without twins, which results in a clear diffraction pattern for accurate interplanar spacing measurement using FFT analysis. As shown in Fig. 2a-c, we obtained TEM images of the single-crystalline FCC nanoparticles that are well oriented along different zone axes. In the TEM selected area, FFT patterns of the FCC structure of Pd were obtained (lower panel of Fig. 2a-c). The interplanar spacing (d_{hkl}) was calculated using FFT of the HRTEM image by measuring the distance between the spots, which was carefully calibrated with respect to a reference (111) silicon (Si) specimen at the same magnification. Moreover, the intensity profile of the TEM image was also taken to reduce the measurement errors (Fig. S7); the average d_{hkl} was determined from the intensity profile across multiple atomic planes. The analysis was conducted for 10 nanoparticles that were oriented with the same zone axis.

First, rGO/Pd/rGO nanolaminates oriented along the [001] zone axis were analysed for quantifying strains. The d_{hkl} of Pd nanoparticles was measured from the FFT spots, and the strain (ε) was then calculated with respect to the bulk Pd reference values (d_0) (Table S1), where $\varepsilon = (d_{hkl}-d_0)/d_0$. From the FFT shown in Fig. 2a, the average interplanar spacing of the {200} family of planes at the [001] zone-axis oriented Pd nanoparticles was determined to be 2.014 Å. This value was larger than that corresponding to the (200) plane, which has a bulk Pd value of 1.945 Å. This indicates that the rGO layers caused a tensile strain to be developed in the in-plane orientation of the Pd

nanoparticles. Within the same [001] zone axis, we also evaluated the interplanar spacing for {220} planes. Similarly, Pd nanoparticles oriented with [011], [112] zone axes were also analysed (Fig. 2b-c). The calculated strain values for Pd nanoparticles of different orientations are summarized in Fig. 2d, which indicates that there was no significant orientation dependency with an average tensile strain of 3.30±0.17% across all orientations.

The rationalization for the tensile strain can be explained in terms of two factors. First, the rGO layer may impose a lateral pulling force in the in-plane orientation due to the chemical interaction with Pd (blue arrows in Scheme 1). Second, the rGO layer encapsulation creates a compressive strain due to clamping force in the direction perpendicular to the rGO plane (red arrows in Scheme 1), which in turn induces a lateral expansion of the nanoparticles in the in-plane direction. These two factors will be explored further below.

Next, to determine the strain induced on the nanoparticles upon hydrogen absorption, the hydrided rGO/PdH_x/rGO nanolaminates were analysed (Fig. 2e-g). Hydrogen absorption was performed under 100 °C and 15 bar of H_2 pressure, and then HRTEM image was taken to determine the strain imposed on the PdH_x nanoparticles. It should be noted that some of PdH_x nanoparticles were partially dehydrided during exposure to air before analysis, which resulted in the coexistence of Pd and PdH_x phases (Fig. S5). Due to the partial hydrogen desorption, it was not possible to determine the reference $d_{0,\text{bulk-PdH}x}$ value for the non-fully hydrided PdH_x, and thus the $d_{0,\text{bulk-Pd}}$ value of bulk Pd was taken as a reference for the initial strain estimates. For example, in calculating the strain induced on the {200} plane of PdH_x along [001] zone axis, the interplanar spacing of (200) bulk Pd of 1.945 Å was used.

The calculated strain values for PdH_x nanoparticles with respect to bulk Pd for different zone axes along different in-plane directions are summarized in Fig. 2h. The average strain for PdH_x nanoparticles based on the results from different zone axes was determined to be 5.44±0.18% (versus bulk Pd); larger than the value for encapsulated Pd reported above (3.30±0.17%). The difference in strain is primarily due to a large lattice expansion of 3.50% upon the phase transformation from the hydrogen-poor (α phase) to the hydrogen-rich (β phase).[28–30] Thus, the tensile strain imposed on PdH_x nanoparticles arises from the combined effect of the phase transformation, as well as the effect of the rGO encapsulation, adding up to a larger value than what was measured for the encapsulated Pd nanoparticles. However, the measured average value of the PdH_x tensile strain (5.44%) is actually smaller than the multiplication product of the measured average strain of Pd upon encapsulation before hydrogen absorption (3.30%) and the expected phase transformation strain for the bulk material (3.50%). This is presumably due to the confining effect provided by the rGO layer during the hydrogen absorption process.

The above initial strain analysis of the experimentally determined d_{hkl} for both Pd and PdH_x in the nanolaminates relies on the value of d_0 for bulk Pd as a reference. However, a more complete and unbiased analysis should incorporate the fact that synthesized Pd nanoparticles are known to exhibit a lattice contraction due to the effect of surface tension upon nanosizing, thus resulting in a different equilibrium lattice spacing in comparison to the bulk counterpart.[26,27] To separate this factor from the impact of encapsulation, atomistic simulations were conducted to determine the expected Pd-Pd interatomic distance as a function of the particle size, based on a combination of first-principles density functional theory (DFT) and classical molecular dynamics (MD) simulations (see Supplementary Information (SI) for details of the computational procedures). The computed percent change in Pd-Pd interatomic distances in Pd and PdH nanoparticles with respect to their bulk counterparts is plotted in Fig. 3. A significant reduction in the interatomic distance and the accompanying lattice parameter are found for particle dimensions below 6 nm, indicating that our initial strain estimate was underestimated when using d_0 values of bulk Pd as a reference.

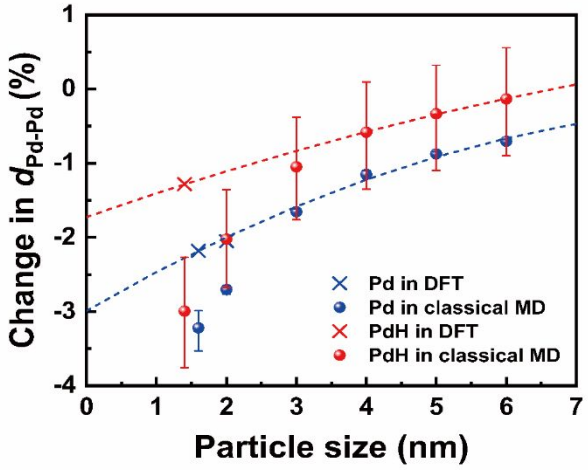

Fig. 3 Predicted changes in Pd-Pd interatomic distance, d_{Pd-Pd}, due to surface tension in unconfined Pd (blue) and PdH (red) nanoparticles. d_{Pd-Pd} was obtained from DFT calculations (x markers) for smaller particles less than 2 nm, while classical MD simulations (circles) were used for larger particles. The expected trends (dashed lines) are drawn from interpolation between the two methods.

For 3 nm Pd and PdH particles, which are similar to the synthesized particle sizes, the surface tension was predicted to reduce the lattice parameters by 1.58% and 0.83% in comparison to the bulk counterparts, respectively. Moreover, the value for $PdH_{0.67}$, which is close to the expected β phase composition,[31] can be linearly interpolated between Pd and PdH, giving an estimated 1.08% reduction in the lattice parameter of nanoscale $PdH_{0.67}$. These values alter the strain of nanolaminates reported above. Specifically, the tensile strain determined for rGO/Pd/rGO nanolaminates with a [011] zone axis along {111} planes was 2.98±0.18% when referenced to the bulk Pd lattice parameter, but a tensile strain of 4.64±0.18% was obtained if the lattice parameter of contracted 3 nm Pd nanoparticles determined from the simulations is used as a reference. For hydrided rGO/PdH_x/rGO nanolaminates of the same [011] zone axis and {111} planes (assuming the $PdH_{0.67}$ composition), the tensile strain was determined to be 5.29±0.40% when referenced to bulk Pd, but revised to 2.84±0.39% if the 3 nm $PdH_{0.67}$ nanoparticle simulation data is used as a reference.

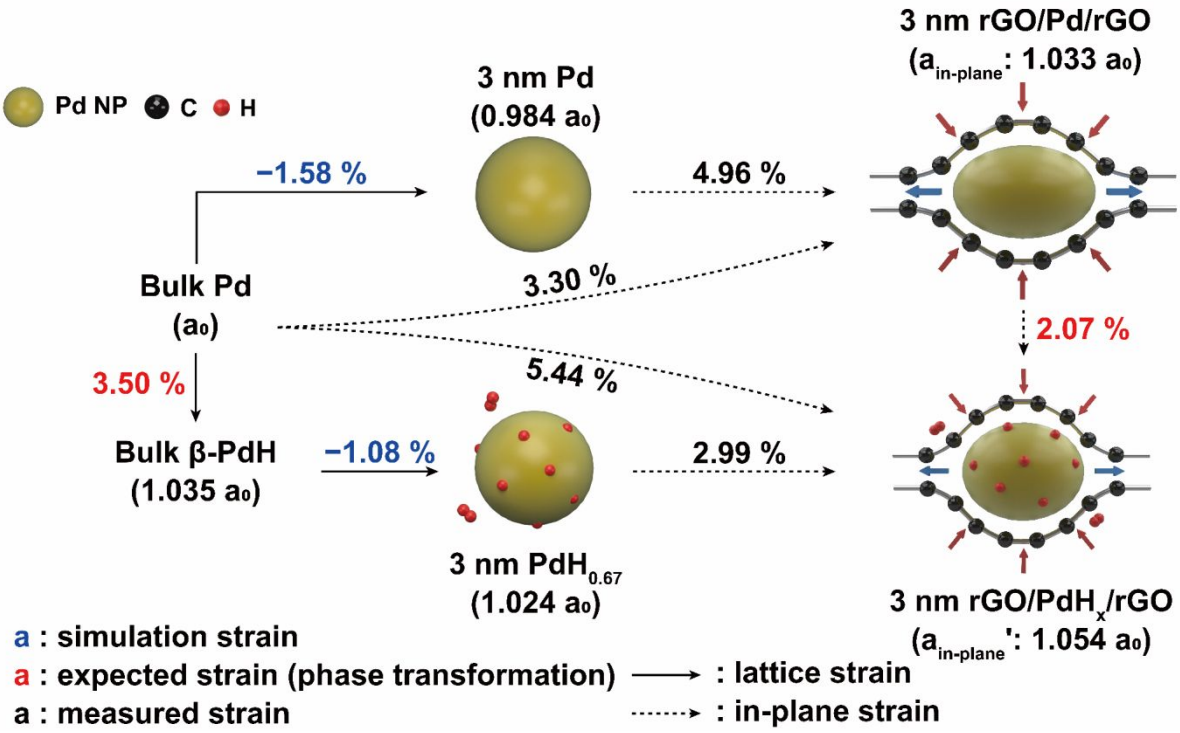

Fig. 4 Flow diagram of in-plane strain values for Pd and PdH_x upon nanosizing and encapsulation, based on a combination of simulation results and experimental TEM measurements. The net average in-plane strain imposed on the Pd and hydrided Pd nanoparticles due to encapsulation is 4.96% and 2.99%, respectively. This indicates a lattice expansion of 2.07% due to the phase transformation upon hydrogen absorption within the encapsulant.

These new values reflect the specific net impact of encapsulation beyond nanosizing.

The in-plane lattice parameter changes from bulk to nanoparticle to rGO/PdH_x/rGO nanolaminates based on the combination of simulation data and TEM analysis are summarized in Fig. 4. The net contributions from the rGO encapsulation and nanosizing cause a significant build-up of strain in both as-synthesized and hydrided rGO/PdH_x/rGO nanolaminates. Moreover, the net lattice expansion due to hydriding is diminished with respect to the bulk, exhibiting only a 2.07% expansion as compared to the expected 3.50% bulk value. Because this strain can affect the thermodynamic reaction enthalpies and/or kinetics, the hydrogen storage properties were measured next to correlate the performance to the induced strain.

Hydrogen storage properties of rGO/Pd/rGO nanolaminates

The kinetics of the hydrogen absorption of neat Pd nanoparticles without rGO encapsulation (bare-Pd) and rGO/Pd/rGO nanolaminates were measured at 100 °C under 2.2 bar of H_2 pressure to investigate the impact of rGO on the hydrogen sorption (Fig. 5a). To solely focus on the PdH_x capacity, the capacity was re-normalized based on Pd mass through inductively coupled plasma (ICP) measurements. While bare-Pd samples absorb less than 0.4 H per Pd atom within 50 min (x<0.4), rGO/Pd/rGO nanolaminates uptake 0.9 H per Pd atom (x=0.9), representing a substantially enhanced hydrogen capacity (see SI for details). Moreover, Pd particles in the nanolaminates exhibit up to 0.57 H absorption per Pd atom within 5 min, which means that rGO/Pd/rGO nanolaminates can absorb hydrogen approximately three times faster than bare-Pd at the initial hydriding stage. Since the Pd particles are in a comparable size regime for both systems (Fig. S1b), this outstanding storage performance can be attributed to the rGO encapsulation effect.

For a quantitative study of the thermodynamic properties of the rGO/Pd/rGO nanolaminates, we conducted PCT measurements at three different temperatures, as shown in Fig. 5b (see Fig. S8 for bulk Pd isotherms). All isotherms show a distinctive plateau pressure, suggesting the coexistence of α and β phase regions. The thermodynamic parameters of nanolaminates, enthalpies (ΔH) and entropies (ΔS), were calculated through van't Hoff plots by fitting a linear regression line. The procedure for determining the equilibrium pressure (P_{eq}) and the corresponding van't Hoff plots are described in detail in Fig. S9 and Fig. S10, respectively. The average enthalpy and entropy between absorption (α→β) and desorption (β→α) reactions, ΔH_{rxn} and ΔS_{rxn}, are summarized in Table 1. Both reaction enthalpy and entropy change increase due to the rGO encapsulation of Pd nanoparticles, $\Delta\Delta H_{rxn}^{rGO}$ = 3.7 kJ (mol H_2)$^{-1}$ and $\Delta\Delta S_{rxn}^{rGO}$ = 10.3 J·K^{-1} (mol H_2)$^{-1}$, which is contrary to the nanosizing effect of bare (free standing) Pd nanoparticles. In addition, the enthalpy hysteresis between absorption and desorption slightly decreases from 5.7 to 5.2 kJ (mol H_2)$^{-1}$ from bulk to the rGO/Pd/rGO nanolaminates. For comparison, the reaction thermodynamic parameters measured for bare (free standing) Pd nanoparticles of similar size are ΔH_{rxn} = 31-34.6 kJ (mol H_2)$^{-1}$ and ΔS_{rxn} = 67.3-83.1 J·K^{-1} (mol H_2)$^{-1}$ from Ref.[9], suggesting that the enthalpy and entropy change decrease due to the nanosizing from bulk (without

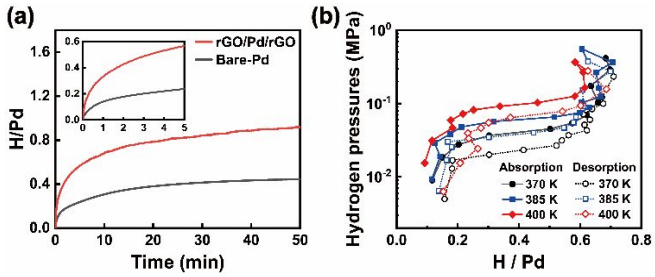

Fig. 5 (a) Hydrogen absorption profiles of rGO/Pd/rGO nanolaminates and bare-Pd at 100 °C under 2.2 bar of H_2 pressure. The inset shows an enlargement for 0-5 min. (b) PCT profiles of rGO/Pd/rGO nanolaminates at three different temperatures.

encapsulation) is $\Delta\Delta H_{rxn}^{nano}$ = −2.8 to −6.4 kJ (mol H_2)$^{-1}$ and $\Delta\Delta S_{rxn}^{nano}$ = −7.7 to −23.5 J·K^{-1} (mol H_2)$^{-1}$. The fact that rGO encapsulation and nanosizing appear to have opposite effects on the ΔH_{rxn} and ΔS_{rxn} suggests that their governing mechanisms to tune thermodynamic behaviors of Pd nanoparticles differ.

Assessment of contributing chemomechanical factors

The reaction enthalpy changes due to rGO encapsulation, $\Delta\Delta H_{rxn}^{rGO}$, can be decomposed into three contributing factors:

$$\Delta\Delta H_{rxn}^{rGO} = \Delta\Delta H_{rxn}^{nano} + \Delta\Delta H_{rxn}^{strain} + \Delta\Delta H_{rxn}^{chem}$$

where $\Delta\Delta H_{rxn}^{nano}$ is the reaction enthalpy difference between nanoparticle and bulk, and $\Delta\Delta H_{rxn}^{strain}$ and $\Delta\Delta H_{rxn}^{chem}$ are the mechanical strain energy and the chemical interaction energy imposed by the rGO encapsulant. In this section, we discuss and assess the contributions of these individual factors and compare the analysis with our PCT measurements in Table 1. First, the impact of strain energy on the reaction enthalpy is assessed. By combining the TEM observation and atomistic simulation, we confirmed that the average in-plane strain induced by the rGO encapsulant is 4.96% and 2.99% for the rGO/Pd/rGO nanolaminates before and after hydrogen absorption, respectively (Fig. 4). Once the out-of-plane strain components and the elastic properties of PdH_x nanoparticles are identified, one can compute the strain energy difference before and after hydrogen absorption, which contributes to the measured reaction enthalpy. As an initial step, we computed the elastic properties of freestanding 3 nm Pd and PdH particles using DFT with an applied external pressure (see the SI for the detailed computational procedure and results). For 3 nm nanoparticles, the bulk moduli were predicted to be reduced upon nanosizing by 42.0% and 41.5%, respectively, resulting in values of 100 GPa (Pd) and 107 GPa (PdH) as shown in Fig. S11.

Next, we proceed to estimate the magnitude of the out-of-plane strain. Because it is complicated to directly measure out-of-plane strain using TEM, we instead introduce a methodology for estimating the range of out-of-plane strain and its associated strain energy. We first need to understand the contributing factors to the measured in-plane strain. As discussed in the strain analysis section, both the clamping force of the rGO layers and the lateral pulling force due to the chemical interaction (red and blue arrows in Scheme 1, respectively) may contribute to the strain. However, the relative amount of their contributions is unknown. We therefore compute two limiting cases: first case in which the out-of-plane strain is entirely a consequence of the clamping force without any lateral pulling force, and second case in which no clamping force is present. The real behavior is assumed to lie between these two limits, and is approximated by linear interpolation of both factors.

Assuming Poisson's ratio, we can easily compute the out-of-plane strain expected for these two limits (see SI for details). The results, along with the interpolation for intermediate cases, are plotted in Fig. 6a. The calculated range of $\varepsilon_{out\text{-}of\text{-}plane}$ is from −1.87% to −13.19% for Pd, and from −1.18% to −7.57% for PdH. Note that values of $\varepsilon_{out\text{-}of\text{-}plane}$ in the limit of 100% clamping force contribution is too high to be realistic. This allows us to conclude that the contribution from the lateral pulling force is in fact non-trivial. The underlying physical motivation for the lateral pulling force is a specific chemical interaction between the nanoparticle and rGO layer.

The strain energy can be calculated by incorporating $\varepsilon_{in\text{-}plane}$, $\varepsilon_{out\text{-}of\text{-}plane}$, and elastic stiffness tensor of nanoparticles according to equation (1-2) in the Experimental section. The reaction enthalpy is shifted by the difference in strain energies, $\Delta H_{strain}^{\alpha} - \Delta H_{strain}^{\beta}$, which is depicted by the gray shaded area in Fig. 6a. Assuming the clamping force induces 30-70% of $\varepsilon_{in\text{-}plane}$, a range of $\Delta\Delta H_{rxn}^{strain}$ is predicted 0.9-2.4 kJ (mol H_2)$^{-1}$. It is worth noting that this calculated strain energy may be underestimated due to the variations in PdH_x nanoparticle orientations and particle sizes, which are not fully reflected. For example, equation (1) takes longitudinal terms (ε_{ii}) while ignoring transverse terms (ε_{ij} where $i \neq j$), only partly accounting for strain elements for obliquely oriented particles.

Next, the energy contribution from the chemical interaction between rGO and PdH_x nanoparticles is estimated. As discussed above, we are able to conclude that the chemical interaction is significant, contributing to a lateral pulling force that impacts the lattice strain. However, in addition to the mechanical effect arising from lateral pulling, the chemical interaction can alter the energetics in more fundamental ways, including charge transfer between Pd and the encapsulant. Indeed, Pd 3d binding

Table 1 Thermodynamic parameters of rGO/Pd/rGO nanolaminates and bulk Pd. ΔH_{rxn} and ΔS_{rxn} refer to the average of the absolute value of enthalpy and entropy between absorption and desorption reactions. $\Delta\Delta H_{rxn}^{rGO}$ and $\Delta\Delta S_{rxn}^{rGO}$ refer to the reaction enthalpy and entropy change from bulk to rGO-encapsulated nanolaminates.

Sample	ΔH [kJ (mol H_2)$^{-1}$]				ΔS [J·K^{-1} (mol H_2)$^{-1}$]			
	$\Delta H_{\alpha\to\beta}$	$\Delta H_{\beta\to\alpha}$	ΔH_{rxn}	$\Delta\Delta H_{rxn}^{rGO}$	$\Delta S_{\alpha\to\beta}$	$\Delta S_{\beta\to\alpha}$	ΔS_{rxn}	$\Delta\Delta S_{rxn}^{rGO}$
rGO/Pd/rGO	−38.5±3.6	43.7±5.7	41.1	3.7	−96.2±9.4	105.9±14.9	101.1	10.3
Bulk	−34.5±0.5	40.2±2.1	37.4		−85.5±1.3	96.0±5.4	90.8	

energy in the XPS spectra is up-shifted (Fig. S12), indicating that the electrons in Pd nanoparticles are transferred to rGO sheets. This same effect was confirmed theoretically using DFT calculations on a graphene-PdH_x particle interface model (Fig. S13). The chemical interaction with the graphene sheet was found to stabilize a Pd nanoparticle containing 141 Pd atoms by 3.80 eV and a PdH nanoparticle containing 87 Pd atoms by 2.87 eV. Because DFT computations on larger particles were prohibitive, the results were scaled to the particle sizes of interest to estimate the impacts on reaction enthalpies (see SI for details of the scaling procedure, which yielded an equivalent stabilization of 4.39 eV for a PdH particle with 141 Pd atoms). We further assumed that the sandwiched structure of rGO/PdH_x/rGO nanolaminates would lead to simultaneous interaction with two encapsulant surfaces; hence, the chemical interaction in rGO/PdH_x/rGO was estimated to be twice that of graphene-PdH_x nanoparticle interface. This procedure resulted in an estimated value of $\Delta\Delta H_{\mathrm{rxn}}^{\mathrm{chem}}$ = 1.61 kJ (mol H_2)$^{-1}$.

Finally, the approximate magnitude of nanosizing effect $\Delta\Delta H_{\mathrm{rxn}}^{\mathrm{nano}}$ is estimated. This value can be derived in part from existing experimental data. In particular, Yamauchi reported the reaction enthalpy change due to nanosizing as $\Delta\Delta H_{\mathrm{rxn}}^{\mathrm{nano}}$ = −2.8 to −6.4 kJ (mol H_2)$^{-1}$ (from bulk to bare nanoparticles) and attributed it to locally weakened Pd-H bond strength.[9,32] Due to the higher surface energy of Pd (81 meV/Å^2) versus PdH (45 meV/Å^2) for the {111} orientation, hydrogen in bare nanoparticles is likely to segregate at the surface to lower the surface energy, as observed in the Pd nanocubes.[33] Therefore, it would be easier to insert/extract hydrogen from these regions compared to the octahedral interstitial sites in bulk, leading to the observed decrease in ΔH_{rxn} ($\Delta\Delta H_{\mathrm{rxn}}^{\mathrm{nano}} < 0$).

Nevertheless, it is not clear that the same behavior would translate to the encapsulated system, for which the chemical interaction with rGO is fairly strong. Accordingly, it is reasonable to assume that dangling bonds on the PdH_x nanoparticle surfaces may be partially passivated. Moreover, the rGO encapsulant exerts an external stress, which can impact the hydrogen segregation tendency. Indeed, the strong adhesion of PdH_x particle to graphene predicted from our DFT calculations suggests that hydrogen does not need to be segregated on the surface to mitigate surface dangling bonds, and that the Pd-H bond strength is likewise not significantly weakened on the surface, thereby weakening the nanosizing effect on reaction enthalpy. The increased reaction entropy of 101.1 J·K^{-1} (mol H_2)$^{-1}$ for rGO/Pd/rGO nanolaminates from 90.8 J·K^{-1} (mol H_2)$^{-1}$ for bulk is also indicative of strongly bound H atoms, supporting this assumption. We therefore conclude that the nanosizing effect on the reaction enthalpy likely lies in the range $-2.8 \ll \Delta\Delta H_{\mathrm{rxn}}^{\mathrm{nano}} \lesssim 0$ kJ (mol H_2)$^{-1}$.

The net enthalpy change measured from PCT, $\Delta\Delta H_{\mathrm{rxn}}^{\mathrm{rGO}}$ = 3.7 kJ (mol H_2)$^{-1}$ (from bulk to rGO-encapsulated nanolaminates), can therefore be successfully interpreted as the diminished nanosizing effect by adhesion with rGO ($-2.8 \ll \Delta\Delta H_{\mathrm{rxn}}^{\mathrm{nano}} \lesssim 0$ kJ (mol H_2)$^{-1}$), coupled with the mechanical and chemical interactions of nanoparticles with rGO encapsulation ($\Delta\Delta H_{\mathrm{rxn}}^{\mathrm{strain}}$: ~ 0.9-2.4 kJ (mol H_2)$^{-1}$, and $\Delta\Delta H_{\mathrm{rxn}}^{\mathrm{chem}}$: ~ 1.61 kJ (mol H_2)$^{-1}$). The results are summarized schematically in the energy diagram in Fig. 6b and in Table S4, including the relative impacts on each phase and their collective impact on the reaction enthalpy. It is notable that all three contributions can be of generally similar magnitude, although the signs of their contributions differ (net negative $\Delta\Delta H$ contributions for the nanosizing versus net positive $\Delta\Delta H$ contributions for the mechanical strain and chemical interaction). This suggests that a strategy that is able to alter these contributions independently could be leveraged for tuning reaction enthalpies either upwards or downwards.

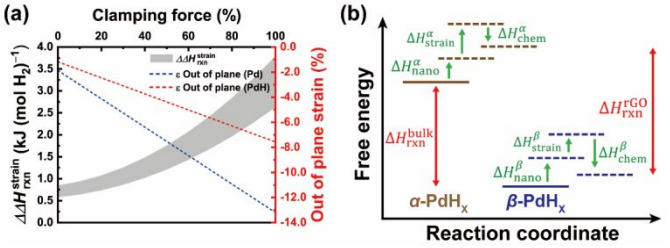

Fig. 6 (a) Ranges of out-of-plane strain and reaction enthalpy changes due to mechanical strain, $\Delta\Delta H_{\mathrm{rxn}}^{\mathrm{strain}}$, calculated according to equation (1-2). (b) Schematic energy diagram of the α and β PdH_x phases, illustrating how the nanosizing, mechanical strain, and chemical interactions with rGO alter the energy state of each individual phase, as well as the overall reaction enthalpy.

It is worth noting that the impact of mechanical strain on the reaction enthalpy depends on the stress state of the system. In a thin film geometry, the clamping of a Pd thin film to a substrate preferentially destabilizes the β phase, and hence the absorption enthalpy decreases while the reaction hysteresis is larger due to the sluggish kinetics.[34] A similar decrease in the absorption enthalpy due to the destabilization of β phase from mechanical strain can be found in other systems, such as Mg[35–38] and the Pd-Ni nanoalloy.[39] However, the rGO/Pd/rGO nanolaminates in this study exhibit mechanical strains not only in the β phase but also in the α phase of PdH_x. Overall, it can be concluded that the interaction with the rGO encapsulant dynamically deforms the Pd nanoparticles during hydrogen absorption, and the net difference in the mechanical response of α and β phases plays a role in tuning its hydrogen storage performance.

Interestingly, the rGO encapsulation also accelerated the absorption kinetics (Fig. 5a) and lowered the absorption and desorption hysteresis (Table 1), even with respect to unconfined Pd nanoparticles. In-plane expansion and out-of-plane compression induced by rGO can produce strain gradient in the PdH_x nanoparticles (Fig. 4), which likely introduces locally extended regions in the rGO/Pd/rGO nanolaminates. Recent studies on the kinetics of PdH_x systems indicate that β phase nucleation is the rate-limiting step for hydrogen absorption, which preferably occurs at the region under tensile strain.[20,40] Facilitated nucleation of the β phase can therefore be attributed to the local extension,[33] as well as to the increased thermodynamic driving force for hydrogen absorption due to the strain energy. In addition, the hydriding of rGO/Pd/rGO requires a smaller lattice expansion of 2.07% compared to the bulk, whereas the expected strain associated with phase

transformation is 3.50% (Fig. 4). A smaller strain may accelerate the growth of the nucleated β phase, which further explains the faster absorption kinetics in the rGO/Pd/rGO nanolaminates.

Conclusions

In this study, we quantified for the first time the strain imposed on Pd nanoparticles within the rGO/Pd/rGO nanolaminates and then correlated the results to the enhancement in hydrogen storage properties. Encapsulation of Pd nanoparticles with rGO layers resulted in a significant build-up of tensile strain and average tensile strain in the in-plane direction was determined as 4.96% and 2.99% before and after hydrogen absorption, respectively. Strain energy was predicted to destabilize the rGO/Pd/rGO nanolaminates more than hydrided one, widening the stability gap between α and β phases by 0.9-2.4 kJ (mol H_2)$^{-1}$. The impact of the chemical interaction reinforces the increase in the reaction enthalpy by stabilizing β phase more than α phase, while the nanosizing effect, which is supposed to reduce the stability gap, was suppressed by adhesion with rGO layers. Finally the net chemomechanical interaction of Pd nanoparticles with the rGO encapsulant increased the stability gap, which was in agreement with the reaction enthalpy change of 3.7 kJ (mol H_2)$^{-1}$ obtained from PCT measurement. These factors contribute meaningfully to the overall changes to reaction thermodynamics, suggesting the possibility of devising a variety of potential improvement strategies. Our findings provide an opportunity to concurrently engineer the stability gap and reaction kinetics *via* chemomechanical interaction with the encapsulant, which opens an interesting avenue for tuning the hydrogen storage performance of metal hydrides.

Conflicts of interest

There are no conflicts to declare.

Acknowledgements

This work was supported by the International Energy Joint R&D Program of the Korea Institute of Energy Technology Evaluation and Planning (KETEP), granted financial resource from the Ministry of Trade, Industry & Energy, Republic of Korea. (No. 20188520000570); KAI-NEET Institute, KAIST, Korea under grant N11200051; and the Hydrogen Materials Advanced Research Consortium (HyMARC) of the U.S. Department of Energy (DOE), Office of Energy Efficiency and Renewable Energy (EERE), Fuel Cell Technologies Office (FCTO) under Contract DE-AC52-07NA27344. This work was partly performed under the auspices of the DOE by Lawrence Livermore National Laboratory (LLNL) under Contract DE-AC52-07NA27344, and the computing resources were provided under the LLNL Institutional Computing Grand Challenge program. The authors appreciate Dr. Kouji Sakaki at AIST for PCT measurements.

Notes and references

1 L. Schlapbach and A. Züttel, *Nature*, 2001, **414**, 353–358.
2 B. Sakintuna, F. Lamari-Darkrim and M. Hirscher, *Int. J. Hydrogen Energy*, 2007, **32**, 1121–1140.
3 S. Singh, S. Jain, V. PS, A. K. Tiwari, M. R. Nouni, J. K. Pandey and S. Goel, *Renew. Sustain. Energy Rev.*, 2015, **51**, 623–633.
4 N. A. A. Rusman and M. Dahari, *Int. J. Hydrogen Energy*, 2016, **41**, 12108–12126.
5 M. Paskevicius, D. A. Sheppard and C. E. Buckley, *J. Am. Chem. Soc.*, 2010, **132**, 5077–5083.
6 A. Schneemann, J. L. White, S. Kang, S. Jeong, L. F. Wan, E. S. Cho, T. W. Heo, D. Prendergast, J. J. Urban, B. C. Wood, M. D. Allendorf and V. Stavila, *Chem. Rev.*, 2018, **118**, 10775–10839.
7 B. C. Wood, V. Stavila, N. Poonyayant, T. W. Heo, K. G. Ray, L. E. Klebanoff, T. J. Udovic, J. R. I. Lee, N. Angboonpong, J. D. Sugar and P. Pakawatpanurut, *Adv. Mater. Interfaces*, 2017, **4**, 1–7.
8 A. Pundt, *Adv. Eng. Mater.*, 2004, **6**, 11–21.
9 M. Yamauchi, R. Ikeda, H. Kitagawa and M. Takata, *J. Phys. Chem. C*, 2008, **112**, 3294–3299.
10 S. Cheung, W. Q. Deng, A. C. T. Van Duin and W. A. Goddard, *J. Phys. Chem. A*, 2005, **109**, 851–859.
11 C. Zhou and J. A. Szpunar, *ACS Appl. Mater. Interfaces*, 2016, **8**, 25933–25940.
12 S. Choi, C. Kim, J. M. Suh and H. W. Jang, *Carbon Energy*, 2019, **1**, 85–108.
13 E. S. Cho, A. M. Ruminski, S. Aloni, Y. S. Liu, J. Guo and J. J. Urban, *Nat. Commun.*, 2016, **7**, 1–8.
14 H. W. Kim, H. W. Yoon, S. Yoon, B. M. Yoo, B. K. Ahn, Y. H. Cho, H. J. Shin, H. Yang, U. Paik, S. Kwon, J.-Y. Choi and H. B. Park, *Science*, 2013, **342**, 91–95.
15 R. K. Joshi, P. Carbone, F. C. Wang, V. G. Kravets, Y. Su, I. V. Grigorieva, H. A. Wu, A. K. Geim and R. R. Nair, *Science*, 2014, **343**, 752–754.
16 M. U. Niemann, S. S. Srinivasan, A. R. Phani, A. Kumar, D. Y. Goswami and E. K. Stefanakos, *J. Nanomater.*, 2008, **2008**, 1–9.
17 Y. Sekimoto, R. Ohtani, M. Nakamura, M. Koinuma, L. F. Lindoy and S. Hayami, *Sci. Rep.*, 2017, **7**, 1–7.
18 H. Nakatsuji and M. Hada, *J. Am. Chem. Soc.*, 1985, **107**, 8264–8266.
19 A. Baldi, T. C. Narayan, A. L. Koh and J. A. Dionne, *Nat. Mater.*, 2014, **13**, 1143–1148.
20 N. J. J. Johnson, B. Lam, B. P. MacLeod, R. S. Sherbo, M. Moreno-Gonzalez, D. K. Fork and C. P. Berlinguette, *Nat. Mater.*, 2019, **18**, 454–458.
21 S. M. Choi, M. H. Seo, H. J. Kim and W. B. Kim, *Carbon N. Y.*, 2011, **49**, 904–909.
22 V. Mazumder and S. Sun, *J. Am. Chem. Soc.*, 2009, **131**, 4588–4589.
23 P. Giannozzi, O. Andreussi, T. Brumme, O. Bunau, M. Buongiorno Nardelli, M. Calandra, R. Car, C. Cavazzoni, D. Ceresoli, M. Cococcioni, N. Colonna, I. Carnimeo, A. Dal Corso, S. de Gironcoli, P. Delugas, R. A. DiStasio, A. Ferretti, A. Floris, G. Fratesi, G. Fugallo, R. Gebauer, U. Gerstmann, F. Giustino, T. Gorni, J. Jia, M. Kawamura, H.-Y. Ko, A. Kokalj, E. Küçükbenli, M. Lazzeri, M. Marsili, N. Marzari, F. Mauri, N. L. Nguyen, H.-V. Nguyen, A. Otero-de-la-Roza, L. Paulatto, S. Poncé, D.

Rocca, R. Sabatini, B. Santra, M. Schlipf, A. P. Seitsonen, A. Smogunov, I. Timrov, T. Thonhauser, P. Umari, N. Vast, X. Wu and S. Baroni, *J. Phys. Condens. Matter*, 2017, **29**, 465901.
24 O. Andreussi, I. Dabo and N. Marzari, *J. Chem. Phys.*, 2012, **136**, 064102.
25 F. D. Murnaghan, *Proc. Natl. Acad. Sci.*, 1944, **30**, 244–247.
26 W. H. Qi and M. P. Wang, *J. Nanoparticle Res.*, 2005, **7**, 51–57.
27 R. Lamber, S. Wetjen and N. I. Jaeger, *Phys. Rev. B*, 1995, **51**, 10968–10971.
28 M. Vadai, D. K. Angell, F. Hayee, K. Sytwu and J. A. Dionne, *Nat. Commun.*, 2018, **9**, 1–8.
29 T. C. Narayan, A. Baldi, A. L. Koh, R. Sinclair and J. A. Dionne, *Nat. Mater.*, 2016, **15**, 768–774.
30 L. W. McKeehan, *Phys. Rev.*, 1923, **21**, 334–342.
31 D. G. Narehood, S. Kishore, H. Goto, J. H. Adair, J. A. Nelson, H. R. Gutiérrez and P. C. Eklund, *Int. J. Hydrogen Energy*, 2009, **34**, 952–960.
32 K. C. Kim, B. Dai, J. Karl Johnson and D. S. Sholl, *Nanotechnology*, 2009, **20**, 204001.
33 A. Ulvestad, M. J. Welland, S. S. E. Collins, R. Harder, E. Maxey, J. Wingert, A. Singer, S. Hy, P. Mulvaney, P. Zapol and O. G. Shpyrko, *Nat. Commun.*, 2015, **6**, 10092.
34 Y. Pivak, H. Schreuders, M. Slaman, R. Griessen and B. Dam, *Int. J. Hydrogen Energy*, 2011, **36**, 4056–4067.
35 S. Hao and D. S. Sholl, *J. Phys. Chem. C*, 2012, **116**, 2045–2050.
36 J. Lu, J. C. Young, Z. F. Zhigang, Y. S. Hong and E. Rönnebro, *J. Am. Chem. Soc.*, 2009, **131**, 15843–15852.
37 D. Khan, J. Zou, S. Panda and W. Ding, *J. Phys. Chem. C*, 2020, **124**, 9685–9695.
38 J. Zhang, C. Mao, J. Chen, C. G. Long, K. Tang, M. J. Zhang and P. Peng, *Comput. Mater. Sci.*, 2015, **105**, 71–74.
39 Y. Oumellal, C. Matei Ghimbeu, A. Martínez de Yuso and C. Zlotea, *Int. J. Hydrogen Energy*, 2017, **42**, 1004–1011.
40 K. Sytwu, F. Hayee, T. C. Narayan, A. L. Koh, R. Sinclair and J. A. Dionne, *Nano Lett.*, 2018, **18**, 5357–5363.